Journal Pre-proof

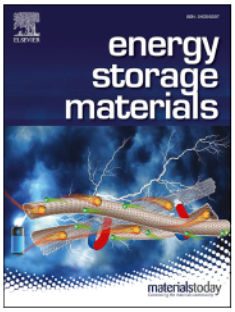

Regulated lithium ionic flux through well-aligned channels for lithium dendrite inhibition in solid-state batteries

Yang Li, Daxian Cao, William Arnold, Yao Ren, Chao Liu, Jacek Jasinski, Thad Druffel, Ye Cao, Hongli Zhu, Hui Wang

PII: S2405-8297(20)30251-8

DOI: https://doi.org/10.1016/j.ensm.2020.06.029

Reference: ENSM 1253

To appear in: *Energy Storage Materials*

Received Date: 2 May 2020

Revised Date: 17 June 2020

Accepted Date: 19 June 2020

Please cite this article as: Y. Li, D. Cao, W. Arnold, Y. Ren, C. Liu, J. Jasinski, T. Druffel, Y. Cao, H. Zhu, H. Wang, Regulated lithium ionic flux through well-aligned channels for lithium dendrite inhibition in solid-state batteries, *Energy Storage Materials* (2020), doi: https://doi.org/10.1016/j.ensm.2020.06.029.

Credit authorship contribution statement

Yang Li: Conceptualization, Methodology, Investigation, Formal analysis, Writing - original draft, Writing - review & editing. **Daxian Cao**: Investigation, Writing - review & editing. **William Arnold**: Investigation, Writing - review & editing. **Yao Ren**: Investigation, Software, Writing - review & editing. **Chao Liu**: Investigation, Writing - review & editing. **Jacek Jasinski**: Investigation, Writing - review & editing. **Thad Druffel**: Writing - review & editing. **Ye Cao**: Investigation, Software, Writing - review & editing. **Hongli Zhu**: Conceptualization, Methodology, Writing - original draft, Writing - review & editing. **Hui Wang**: Conceptualization, Methodology, Writing - original draft, Writing - review & editing, Project administration.

Regulated Lithium Ionic Flux through Well-Aligned Channels for Lithium Dendrite Inhibition in Solid-State Batteries

Yang Li [a], Daxian Cao [b], William Arnold [a,c], Yao Ren [d], Chao Liu [b], Jacek Jasinski [a], Thad Druffel [a], Ye Cao [d], Hongli Zhu [b,*], Hui Wang [a,c,*]

[a] Conn Center for Renewable Energy Research, University of Louisville, 216 Eastern Parkway, Louisville, KY 40292, USA

[b] Department of Industrial and Mechanical Engineering, Northeastern University, 360 Huntington Ave, Boston, MA 02115, USA

[c] Department of Mechanical Engineering, University of Louisville, 332 Eastern Parkway, Louisville, KY 40292, USA

[d] Department of Materials Science and Engineering, The University of Texas at Arlington, Arlington, TX 76019, USA

*Corresponding Author: Hongli Zhu (h.zhu@neu.edu); Hui Wang (hui.wang.1@louisville.edu).

Table of Content Graphic

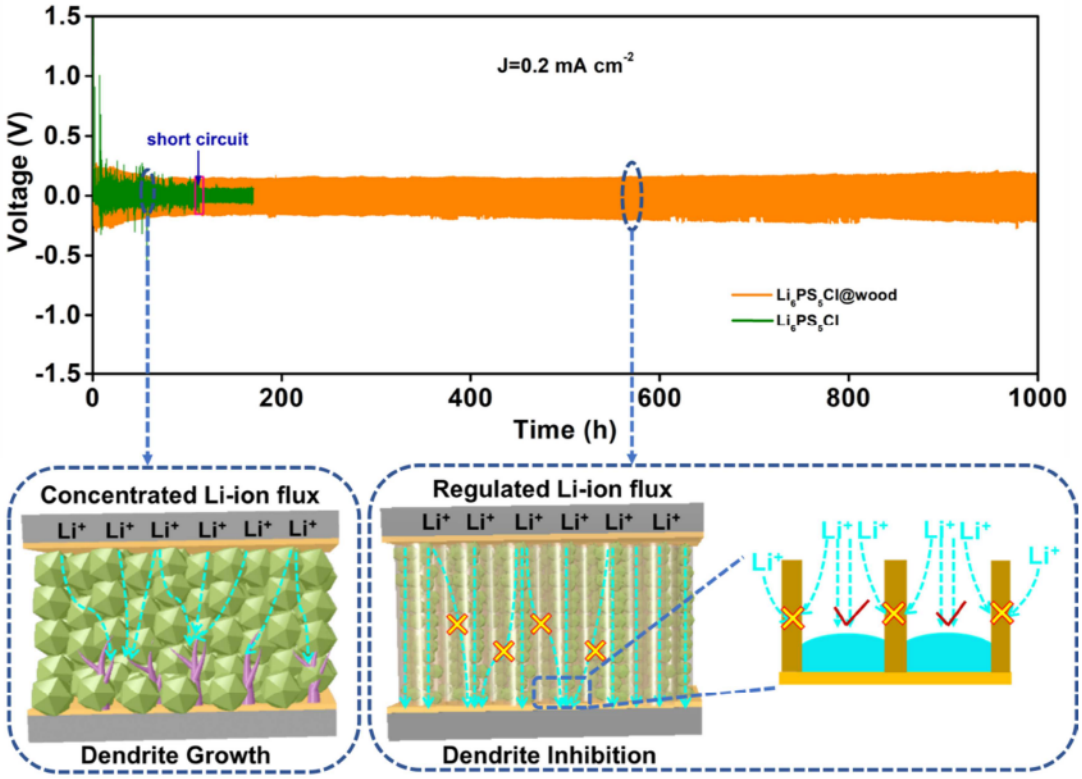

A novel strategy to suppress lithium dendrites in solid-state electrolytes is designed *via* regulating homogeneous Li ionic flux through vertically aligned channels, facilitating a uniform Li electrodeposition.

Regulated Lithium Ionic Flux through Well-Aligned Channels for Lithium Dendrite Inhibition in Solid-State Batteries

Abstract

The utilization of solid electrolyte (SE) to suppress lithium (Li) dendrites is promising but still far from satisfactory due to the inhomogeneous Li plating/stripping. Here, we demonstrated a novel strategy to inhibit Li dendrites *via* regulating Li-ion flux in SE by using vertically aligned channels. The ion-insulating walls facilitated uniform distribution of Li-ion flux through the channels, leading to a homogeneous Li deposition, thus alleviating Li dendrite formation. As a result, symmetric cells with this SE exhibited excellent long-term stability (1000 h) against Li metal. In addition, $Li_4Ti_5O_{12}$ (LTO)/Li cell with the developed SE achieved good battery performance over 100 cycles. The mechanism for dendrite suppression was further investigated by phase-field simulation. This provides a novel strategy by manipulating uniform Li-ion flux to fabricate SE to inhibit Li dendrites and facilitates the development of high-performance rechargeable Li batteries.

Keywords: regulated Li-ion flux, aligned channels, Li dendrite inhibition, solid electrolyte, stable cycling, Li metal battery

1. Introduction

The growing demand for portable devices, electric vehicles (EVs) and grid energy storage systems requires a major breakthrough on safer, high-energy-density battery technologies [1−3]. Lithium (Li) metal is being regarded as the ultimate choice for anode material owing to the extra-high specific capacity (3,860 mAh g^{-1}), the lowest negative electrochemical potential (−3.040 V *vs.* standard hydrogen electrode), and the light-weight (0.53 g cm^{-3}) [4−6]. Unfortunately, the utilization of Li metal with the most conventional liquid or polymer electrolytes is unsatisfactory due to the unavoidable Li dendrites that can penetrate the separator, thus causing an internal short circuit of a cell during operation [7,8]. Solid electrolytes (SEs) have emerged as very attractive alternatives as they offer a promising approach to solve the safety issues induced by Li dendrites due to their inherent nonflammability and mechanical hardness [9,10].

Considerable research efforts have been devoted in exploring different types of superionic SEs, such as perovskite-type [11], antiperovskite-type [12], thio-LiSICON-type [13], NASICON-type [14,15], garnet [16], and sulfide-based glass/ceramic [17]. The ionic conductivity of several SEs (10^{-4}–10^{-3} S cm^{-1} at room temperature) can be comparable to the value of liquid electrolytes [18,19]. However, instead of suppressing Li dendrites, SEs suffer from low critical current density (CCD) (<1.0 mA cm^{-2}) [20−22] and abrupt short circuits still happen for SEs or even worse than those in liquid electrolytes [23]. Although the mechanism for Li dendrite propagation in SEs is not fully understood, it is widely believed that Li dendrites first

nucleate at the defect-rich areas of SE/Li interface, and then propagate along the grain boundaries or through the voids between ceramic particles [24]. Consequently, in order to suppress the Li dendrites, SE pellets with high density have been prepared to reduce the inhomogeneous current density distribution which is essential for dendrite formation/growth [25,26]. However, perfect SE pellets without defects are too ideal and highly challenging for materials preparation. Based on the fundamental studies of dendrite formation/growth [27,28], many attempts have been made to inhibit dendrites, including the modification of SEs (e.g., increase grain boundary conductivity) [29,30], and the stabilization of SE/Li interface by introducing a buffer layer (fluorinated compounds [31], Li polysulfide [32], $LiNO_3$ [33], ionic liquids and cross-linked network polymer electrolytes [34]). Although the artificial buffer layer can enhance the interfacial stability to suppress Li dendrites in different levels [35−37], the intrinsic problem of uneven Li electrodeposition remains unsolved.

Since inhomogeneous Li stripping/plating is considered to be one of the major reasons for the dendrite formation/growth at interface [38−40], thus, we hypothesize that manipulating the SE structure by facilitating a uniform Li nucleation and growth could be an effective approach for Li dendrite inhibition. As shown in **Scheme 1a**, nonuniform Li-ion flux induces the formation of Li dendrites in bare SEs, as it normally accelerates inhomogeneous Li stripping/plating at the spots where the current density is locally enhanced. Such spots then tend to attract more Li ions, leading to further growth of the nucleus and finally evolving into dendrites [41−43]. In contrast, as presented in **Scheme 1b**, for the SE structure with vertically aligned

channels, homogeneous Li stripping/plating could be expected. The uniformly aligned channels could help form a well-distributed Li ionic flux through each channel, leading to a uniform Li deposit and dissolution. Moreover, Li ions tend to transport along vertical directions rather than randomly scattered directions due to the restriction from insulating walls, preventing the accumulation and uncontrolled magnification of Li deposition.

Herein, we demonstrated our hypothesis through a novel approach for the suppression of Li dendrites *via* regulating homogeneous Li ionic flux over Li metal by ion-insulating confinements, facilitating a uniform Li electrodeposition. Therefore, the Li deposit was not able to evolve into dendritic structures like those in the bare SE. Consequently, the symmetric cells with this SE structure exhibited outstanding long-term stability (up to 1000 h) against Li metal at the current density of 0.2 mA cm^{-2}. In addition, $Li_4Ti_5O_{12}$ (LTO)/Li cell with the developed SE delivered good battery performances over 100 cycles. The mechanism for the dendrite suppression was further investigated through a computational approach with phase-field model (PFM). This indicates that manipulating uniform Li-ion flux in SE is able to inhibit Li dendrites and facilitates the development of high-performance rechargeable Li batteries.

2. Results and Discussion

In this work, we chose wood as the model template material because it naturally possesses well-aligned channels for water/mineral transportation from underground to

leaves during metabolism process. Wood templates, as functional materials [44], have been used to fabricate electrodes, electrolytes or current collectors for various batteries [40,45−48]. Composite electrolytes with ceramic nanowires [49,50] or aligned nanochannels [51,52] have been reported in recent works to enhance the ionic conductivity. However, using well-aligned template to prepare sulfide solid electrolyte to suppress Li dendrite by the regulation of Li-ion flux has not been reported. Here, we prepared Li_6PS_5Cl-infused wood SE (Li_6PS_5Cl@wood) by vacuum-assisted sol-gel infusion method followed by a low temperature heat treatment (<200 °C) for drying (**Scheme 2**). Li_6PS_5Cl was chosen as the SE because of the high ionic conductivity (>10^{-4} S cm^{-1} at room temperature) of argyrodite-type crystals with cubic structure (space group *F-43m*) [53].

The morphology and microstructure of the wood template and Li_6PS_5Cl@wood SE were characterized by scanning electron microscopy (SEM). The top-view SEM image in **Fig. 1a** shows that the wood template exhibits highly uniform porous structures. The SEM images of cross-section (**Fig. 1b** and **1c**) further display the well-defined, aligned and elongated channels with average diameters of around 15 μm throughout the wood template (**Fig. S1a** and **S1b**), which is beneficial for the infusion of Li_6PS_5Cl precursor into the channels. After infusing Li_6PS_5Cl into wood template, the surface morphology of the SE (**Fig. 1d**) becomes totally different, whereas Li_6PS_5Cl particles fully covered the wood surface. The cross-sectional SEM images in **Fig. 1e** and **1f** further confirm the incorporation of Li_6PS_5Cl particles into the channels of wood template. **Fig. 1f** clearly reveals that aligned channels of the wood

template are filled with Li_6PS_5Cl particles. Furthermore, the elemental mapping images by energy dispersive spectroscopy (EDS) (**Fig. 1g**) demonstrate the uniform distributions of phosphorous (P), sulfur (S) and chloride (Cl) inside the wood channels, implying that the Li_6PS_5Cl was fully infused into the channels of wood template, which provides fast Li-ion transport pathways. The success of SE infusion into wood template is attributed to the good solubility of liquid-synthesized Li_6PS_5Cl in anhydrous ethanol [54], as well as the vacuum-assisted sol-gel infusion method.

Fig. 2a displays the X-ray diffraction (XRD) patterns of pure Li_6PS_5Cl, wood template and Li_6PS_5Cl@wood. For pure Li_6PS_5Cl, the sharp diffraction peaks 2θ=15, 18, 25, 30 and 31° are assigned to the cubic structure of Li_6PS_5Cl argyrodite (space group *F-43m*) [53, 55]. Since wood is composed of hemicellulose, amorphous lignin and cellulose, the XRD of wood exhibits a similar crystalline structure to cellulose, in detail, 2θ=22° corresponds to the (002) crystalline plane of cellulose [56]. In the XRD patterns of Li_6PS_5Cl@wood, the characteristic peaks of Li_6PS_5Cl are well maintained. X-ray photoelectron spectroscopy (XPS) was employed to further examine crystalline Li_6PS_5Cl in Li_6PS_5Cl@wood SE (**Fig. 2b**). Beside O 1s (531 eV) and C 1s (284.5 eV) peaks, the main peaks at 198.5, 164, 129.9 and 55.6 eV are mainly ascribed to Cl 2p, S 2p, P 2p and Li 1s, respectively, which corresponds to Li_6PS_5Cl [57]. Both XRD and XPS results suggest that there is no chemical reaction between Li_6PS_5Cl argyrodite and wood template. Thermogravimetric analysis (TGA) was performed to investigate the thermal stability of the samples. In **Fig. S2a**, a remarkable weight reduction that appeared between 180°C and 350 °C is due to the decomposition of

wood components, with weight loss of 78 wt% for wood template and 35 wt% for Li_6PS_5Cl@wood, respectively. In addition, Li_6PS_5Cl in Li_6PS_5Cl@wood starts to gradually decompose from around 360 °C (**Fig. S2b**). The amount of Li_6PS_5Cl infused in the wood structure is around 46 wt%.

The Li^+ conductivity of the electrolytes from room temperature to 90 °C was investigated and shown in **Fig. 2c**. Li_6PS_5Cl@wood SE displays an ionic conductivity of 2.2×10^{-4} S cm^{-1} at room temperature, which is slightly lower than that of pure Li_6PS_5Cl SE (3.4×10^{-4} S cm^{-1}). The good ionic conductivity of Li_6PS_5Cl@wood SE is due to the formation of continuous and fast Li-ion transport pathways as a result of Li_6PS_5Cl infusion in well-aligned channels in the wood structure. In addition, the activation energy (E_a) calculated from Arrhenius plot for Li_6PS_5Cl@wood SE is 0.28 eV which is smaller than that of Li_6PS_5Cl SE (0.34 eV). The lower activation energy indicates that the temperature dependence of Li-ion movement in Li_6PS_5Cl@wood is not as sensitive as that in Li_6PS_5Cl. The impedance spectra of Li_6PS_5Cl and Li_6PS_5Cl@wood solid electrolytes at various temperatures of 30, 60 and 90 °C were measured as shown in **Fig. 2d**.

To identify the interface stability with metallic Li anode, galvanostatic cycling were performed on symmetric Li cells (Li|Li_6PS_5Cl@wood|Li and Li|Li_6PS_5Cl|Li). **Fig. 3a** displays typical voltage profiles of symmetric cells with Li_6PS_5Cl and Li_6PS_5Cl@wood SEs at constant current density of 0.2 mA cm^{-2}. For Li_6PS_5Cl, the voltage profile fluctuates from the initial cycles. After 112 h cycles, an obvious sharp drop in voltage is observed, indicating the internal short circuit formation due to the

severe Li dendrite growth [58]. This is consistent with the previous studies that sulfide SEs suffer from low CCD and cannot suppress Li dendrites even at a low current density [23,24]. In contrast, the symmetric cell with Li_6PS_5Cl@wood SE exhibited very stable voltage profile and 10 times longer cycle lifetime (up to 1000 h) under the same current density (0.2 mA cm^{-2}). Such extended cycling period could be ascribed to the stable interface formed between Li_6PS_5Cl@wood SE and Li metal [31]. The observed arc and plateau in the charge-discharge curve was possibly related to the Li deposition morphology formed on Li metal surface [27,28]. **Fig. 3b** displays that the impedance of the cell with Li_6PS_5Cl@wood SE slightly decreased after cycling due to the improved interfacial properties [59]. However, the impedance of the cell with Li_6PS_5Cl electrolyte after cycling indicates a typical short circuit (**Fig. 3c**). The surface morphologies of Li metal and SE after cycling at 0.2 mA cm^{-2} (after 1000 Li stripping/plating cycles for Li_6PS_5Cl@wood and after about 180 cycles for bare Li_6PS_5Cl) were observed by SEM (**Fig. S3a**–**S3g**). The pristine Li metal displays a smooth and clear surface (**Fig. S3a**). However, the surfaces of Li metal and electrolyte in contact with Li_6PS_5Cl SE after cycling are not uniform, and massive irregular Li dendrites can be observed (**Fig. S3b** and **S3c**). In contrast, the cell with Li_6PS_5Cl@wood SE after cycling shows smoother and more uniform surfaces, and no evidence of Li dendrite formation was found (**Fig. S3d** and **S3e**). The cross sections of Li_6PS_5Cl@wood SE in **Fig. S3f** and **S3g** display that the channel structure filled with Li_6PS_5Cl particles remained good contact after cycling. In addition, the symmetric cell with Li_6PS_5Cl@wood SE was cycled under various current densities

of 0.1, 0.2, 0.5, 0.8 and 1.0 mA cm^{-2}, which correspond to the areal capacities of 0.05, 0.1, 0.25, 0.4 and 0.5 mAh cm^{-2}, respectively (**Fig. 3d**). With increasing current density, the voltage hysteresis gradually increased due to the polarization effect, but still remained stable without obvious polarization amplifying even at 1.0 mA cm^{-2} (0.5 mAh cm^{-2}), revealing good cycling stability and excellent ability to inhibit Li dendrite at high current density. These results suggest that Li_6PS_5Cl@wood SE is effective to restrain the Li dendrite formation/growth, which could be due to the uniform Li-ion flux originating from the confinements of well-aligned channels.

Battery performance of Li_6PS_5Cl@wood SE was evaluated in an LTO/Li cell (**Fig. S4**). It is shown that the cell cycled at 0.2 C delivered a high and stable specific capacity of around 123 mAh g^{-1} with coulombic efficiency of ~99.9% in the whole cycle process (**Fig. S4a**). When increasing the current rate to 0.5 C, the cell still can maintain a high specific capacity over 100 cycles (**Fig. S4b**). **Fig. S4c** displays the charge/discharge curves of the cell under the current rate of 0.5 C at the 1^{st}, 10^{th}, 20^{th}, 50^{th} and 100^{th} cycles, all of which display typical discharge/charge plateaus of the LTO/Li cell at around 1.55 V. In addition, the rate capability of the LTO/Li cell was investigated at various current rates of 0.2 C, 0.5 C, 0.8 C and 1 C. **Fig. S4d** shows that the discharge capacity decreases with increasing current rate due to the polarization effect. Even at a relatively high current rate of 1 C, a decent capacity of 70 mAh g^{-1} still can be obtained. Moreover, the cell exhibited an ability to recover its capacity when the current rate decreased from 1 C to 0.2 C after 20 discharge/charge cycles. The good battery performance could be ascribed to the excellent ability for

inhibiting Li dendrite and high ionic conductivity enabled by Li_6PS_5Cl@wood SE with aligned channels, which indicates the potential application of the developed SE in Li batteries.

Interfacial properties between Li_6PS_5Cl@wood SE and Li metal were inspected and analyzed by XPS after symmetric cell testing at 0.2 mA cm^{-2}. **Fig. 4** displays the XPS spectra fits of Cl 2p, P 2p and S 2p for Li_6PS_5Cl@wood SEs before and after cycling. The Cl 2p spectra show a unique characteristic of Cl^- ions of argyrodite after cycling, suggesting no chemical change of Cl^- ions. The P 2p and S 2p signals before cycling correspond to the PS_4-tetrahedra, the P−S−Li and the P=S bonding motives [57]. After cycling, the formation of reduced phosphorus species, lithium phosphide (Li_3P) and lithium sulfide (Li_2S) are observed, meaning that the reaction between Li_6PS_5Cl and Li could form interphase layer containing new species, such as Li_2S and Li_3P. This observation is consistent with previous report [57] on the interfacial reactivity between pure Li_6PS_5Cl and Li metal. The possible reaction equation as below: $Li_6PS_5X + 8\ Li \rightarrow 5\ Li_2S + Li_3P + LiX$ (X= Cl, Br, I).

The reaction product of LiCl is expected but cannot be detected by the XPS due to the small binding energy difference between LiCl and Cl^- in the argyrodite [57,60]. However, the observation of Li_2S and Li_3P can be the side evidence for LiCl formation. Moreover, as a major product of solid electrolyte interphase (SEI) layer, Li_2S exhibits a relatively high ionic conductivity (~10^{-5} S cm^{-1}) and poor electronic conductivity, which would greatly benefit for the interphase properties of SEI. In addition, SEI layer with high-ion-conducting Li_2S favors uniform Li deposition with

higher nuclei size, which are less likely to pierce SEI, inhibiting the uneven growth of Li dendrites [61].

To further understand the mechanism of the suppression of Li dendrites in Li_6PS_5Cl@wood SE, we performed phase-field simulation to study the Li deposition in SE without and with the channel structure. The simulation system is a 2-dimensional standard half-cell with planar Li metal anode and SE, described by a phase-field variable (ξ), where ξ is equal to 1.0/0.0 for Li metal/SE [62], as illustrated in **Fig. S5a**. In bare SE, Li deposition on Li surface is highly inhomogeneous, causing fast growth of Li dendrites with different length and width. Splits of Li can also be seen at the tip of the dendrites, while voids (dead Li) are formed due to the lateral growth and merge of the Li dendrites, both of which are detrimental to the performance of Li metal batteries (**Fig. 5a**). On the other hand, with insulating template (i.e. wood), Li electrodeposition becomes highly homogeneous. The deposits are strictly confined inside each channel that contains solid electrolyte and not able to evolve onto dendritic structure. The side growth of the Li deposits is suppressed, and no voids are formed (**Fig. 5d**). To further understand this difference, the distribution of Li ion concentration and its flux were analyzed. In bare SE, Li metal/electrolyte interface is curved, where Li ion concentration changes from 0.0 mol L^{-1} (in Li metal) to 1.0 mol L^{-1} (in electrolyte) across that interface (**Fig. S5c**). This induces Li ion flux in both vertical and lateral directions, which accounts for the tip split and void formation during Li dendrite growth. It is also seen that the flux along both directions are inhomogeneous (**Fig. 5b**), which is responsible for the Li dendrite growth. In

contrast, with template, a flat interface between low and high Li ion concentration regions are clearly seen (**Fig. S5d**), and the Li ion transport is only along vertical direction (**Fig. 5e**) while the lateral flux is negligible (**Fig. 5f**). The vertical Li ion flux is homogeneous, as compared with those without template. As a result, the Li deposits become highly homogeneous of equal length and width. The simulation results imply that the introduction of a template with aligned and conductive channels separated by insulating walls can effectively inhibit the Li dendrite growth by confining the Li deposits inside the channels, reducing the lateral Li ion flux and limiting the side growth of Li deposits.

3. Conclusions

In summary, we designed and fabricated a novel SE structure with inorganic sulfide infusion in well-aligned channels to suppress Li dendrites. The model SE was prepared by infusing Li_6PS_5Cl electrolyte into the channels of wood template using a vacuum-assisted sol-gel infusion method. The obtained Li_6PS_5Cl@wood SE shows a superior ionic conductivity of 2.2×10^{-4} S cm^{-1} at room temperature. Moreover, well-aligned channels in Li_6PS_5Cl@wood SE result in regulated Li ionic flux and facilitates a homogenous Li striping/plating behavior during cycling. As a result, a long-term cycling stability up to 1000 hours has been achieved for the Li_6PS_5Cl@wood SE. In addition, LTO/Li cell with the developed SE delivered good battery performances over 100 cycles. The phase-field simulation revealed that introducing a template with aligned channels separated by insulating walls could

effectively inhibit the Li dendrite growth by confining the Li deposits inside the channels, reducing the lateral Li ion flux and limiting the side growth of Li deposits. These features indicate that the strategy of manipulating uniform Li-ion flux to suppress Li dendrites is a promising approach to develop advanced solid electrolytes for high-performance Li batteries.

4. Experimental Section

4.1. Materials

Lithium sulfide (Li_2S) (99.9%, Alfa Aesar), phosphorus pentasulfide (P_2S_5) (98%, Acros Organics), lithium chloride (LiCl) (99%, Alfa Aesar), ethanol (99%, Merck), tetrahydrofuran (THF) (99%, VWR), propylene carbonate (PC) (99%, VWR), bis(trifluoromethanesulfoneimide) lithium salt (LiTFSI), (99.99%, VWR), polyvinylidenedifluoride (PVDF) (99.9%, Sigma-Aldrich), N-methylpyrrolidone (NMP) (99.9%, Sigma-Aldrich) were used as purchased without further purification.

4.2. Synthesis of Li_6PS_5Cl solid electrolyte (SE)

Li_6PS_5Cl SE was synthesized by our previous method.[54] First, β-Li_3PS_4 was prepared following Liang's work [63], in which Li_2S reacts with P_2S_5 in tetrahydrofuran (THF) medium, followed by filtration and heat treatment at 80°C and 140°C under vacuum. To obtain Li_6PS_5Cl, stoichiometric ratio of Li_2S, Li_3PS_4 and LiCl (1:1:1) was used. Li_2S and LiCl were mixed in ethanol and then Li_3PS_4 was added into the solution. Next, the mixture was heated at 90 and 200 °C under vacuum to get the final product.

4.3. Preparation of wood template

Wood templates were prepared by the previous reported method. In typical, wood blocks were cut into slices with thickness of 1.5 mm using a bench saw and boiled in dilute ammonia solution (5 wt %) for 5 h to get rid of lignin inside and enhance the channel connectivity of templates for the following sol infusion. The lignin-extracted wood slices were washed by DI water followed by pure ethanol three times, respectively, and then dried in vacuum oven overnight for the following use.

4.4. Preparation of Li_6PS_5Cl@wood SE

The Li_6PS_5Cl@wood SE structure was fabricated *via* a facile vacuum-assisted sol-gel infusion method followed by a calcination process. To infuse Li_6PS_5Cl into wood template, Li_6PS_5Cl powder was first dissolved in anhydrous ethanol (>100 mg mL^{-1}) to form a homogeneous solution. The prepared wood slices were then immersed into the above solution and magnetically stirred overnight. Subsequently, the solution was heated at 80 °C under vacuum to evaporate the ethanol, and then dried at 180 °C for 1.5 h. Finally, the Li_6PS_5Cl-infused wood slice was further treated at 80 °C for 12 h in a vacuum oven and stored in an argon (Ar) filled glove box (<1 ppm H_2O and O_2) for further use.

4.5. Characterizations

The morphology of the sample was examined using a TESCAN Vega3 scanning electron microscope (SEM). X-ray diffraction (XRD, Bruker D8 Discover) with nickel-filtered Cu Kα radiation (λ = 1.5418 Å) was used for phase identification in the

2θ range of 10° to 70°. Thermogravimetric analysis (TGA) of samples was performed under nitrogen (N_2) atmosphere with a heating rate of 10°C min^{-1} using a TA 2050 system. X-ray photoelectron spectroscopy (XPS) spectra was recorded using Thermo VG Scientific ESCALAB XI X-ray photoelectron spectrometer microprobe.

For the electrochemical measurement, SE pellet was prepared by cold pressing a Li_6PS_5Cl-infused wood slice under ~125 MPa and then placing the slice in a coin cell. The prepared Li_6PS_5Cl@wood SE was sandwiched between two carbon-coated aluminum (Al) foils to determine the ionic conductivity from room temperature to 90 °C. The thickness of prepared Li_6PS_5Cl@wood electrolyte is 700−900 μm. Electrochemical impedance spectroscopy (EIS) was carried out using a Bio-Logic VSP300 electrochemical workstation in the frequency range from 0.1 to 10^6 Hz with an amplitude of 100 mV. The galvanostatic cycling test was conducted with a symmetric Li|Li_6PS_5Cl@wood|Li cell using the same electrochemical workstation at various current densities. The electrochemical performance of the electrolyte was tested with $Li_4Ti_5O_{12}$ (LTO)/Li cells. To prepare the electrode, LTO nanopowder, PVDF and Super P (80:10:10 in weight ratio) were mixed in N-methylpyrrolidone (NMP) to form a homogeneous slurry which was subsequently coated on aluminum foil. The prepared electrode with an active material loading of around 1.5–2.0 mg cm^{-2} was dried at 80 °C for 24 h under vacuum prior to use. Prior to full cell testing, <5 μL PC/LiTFSI electrolyte was added on both sides of the Li_6PS_5Cl@wood SE to enhance interfacial properties. Charge and discharge tests were performed over

1.0–3.0 V after the cells were rested for 8 h. All the symmetric cell and full cell tests were carried out at room temperature.

Declaration of competing interest

The authors declare that they have no competing interests.

Credit authorship contribution statement

Yang Li: Conceptualization, Methodology, Investigation, Formal analysis, Writing - original draft, Writing - review & editing. **Daxian Cao**: Investigation, Writing - review & editing. **William Arnold**: Investigation, Writing - review & editing. **Yao Ren**: Investigation, Software, Writing - review & editing. **Chao Liu**: Investigation, Writing - review & editing. **Jacek Jasinski**: Investigation, Writing - review & editing. **Thad Druffel**: Writing - review & editing. **Ye Cao**: Investigation, Software, Writing - review & editing. **Hongli Zhu**: Conceptualization, Methodology, Writing - original draft, Writing - review & editing. **Hui Wang**: Conceptualization, Methodology, Writing - original draft, Writing - review & editing, Project administration.

Acknowledgments

The authors thank the support from Conn Center for Renewable Energy Research, and the EVPRI Internal Grant of the University of Louisville. W. A. thanks for the Graduate Fellowship supported by NASA Kentucky under NASA award No. NNX15AR69H. H. Z. acknowledge the financial support from the National Science

Foundation under award No. 1924534 and 1933051. H. Z. acknowledge the Kostas Nanomanufacturing Research Center for sharing the Scanning electron microscope.

Appendix A. Supplementary data

Supplementary data to this article can be found online.

Data Availability

The raw/processed data required to reproduce these findings cannot be shared at this time as the data also forms part of an ongoing study.

References

[1] B. Dunn, H. Kamath, J.-M. Tarascon, Electrical energy storage for the grid: a battery of choices, Science 334 (2011) 928–935.

[2] J. B. Goodenough, K.-S. Park, The Li-ion rechargeable battery: a perspective, J. Am. Chem. Soc. 135 (2013) 1167–1176.

[3] J. W. Choi, D. Aurbach, Promise and reality of post-lithium-ion batteries with high energy densities, Nat. Rev. Mater. 1 (2016) 16013.

[4] M. Armand, J.-M. Tarascon, Building better batteries, Nature 451 (2008) 652.

[5] H. Kim, G. Jeong, Y.-U. Kim, J.-H. Kim, C.-M. Park, H.-J. Sohn, Metallic anodes for next generation secondary batteries, Chem. Soc. Rev. 42 (2013) 9011–9034.

[6] D. Lin, Y. Liu, Y. Cui, Reviving the Lithium metal anode for high-energy batteries, Nat. Nanotechnol. 12 (2017) 194.

[7] P. Albertus, S. Babinec, S. Litzelman, A. Newman, Status and challenges in enabling the lithium metal electrode for high-energy and low-cost rechargeable

batteries, Nat. Energy 3 (2018) 16.

[8] W. Xu, J. Wang, F. Ding, X. Chen, E. Nasybulin, Y. Zhang, J.-G. Zhang, Lithium metal anodes for rechargeable batteries, Energ. Environ. Sci. 7 (2014) 513−537.

[9] A. Manthiram, X. Yu, S. Wang, Lithium battery chemistries enabled by solid-state electrolytes, Nat. Rev. Mater. 2 (2017) 16103.

[10] K. K. Fu, Y. Gong, B. Liu, Y. Zhu, S. Xu, Y. Yao, W. Luo, C. Wang, S. D. Lacey, J. Dai, Toward garnet electrolyte-based Li metal matteries: an ultrathin, highly effective, artificial solid-state electrolyte/metallic Li interface, Sci. Adv. 3 (2017) 1601659.

[11] J. F. Ihlefeld, P. G. Clem, B. L. Doyle, P. G. Kotula, K. R. Fenton, C. A. Apblett, Fast lithium- ion conducting thin- film electrolytes integrated directly on flexible substrates for high- power solid- state batteries, Adv. Mater. 23 (2011) 5663−5667.

[12] X. Lü, J. W. Howard, A. Chen, J. Zhu, S. Li, G. Wu, P. Dowden, H. Xu, Y. Zhao, Q. Jia, Antiperovskite Li_3OCl superionic conductor films for solid- state Li- ion batteries, Adv. Sci. 3 (2016) 1500359.

[13] S. Muy, J. C. Bachman, L. Giordano, H.-H. Chang, D. L. Abernathy, D. Bansal, O. Delaire, S. Hori, R. Kanno, F. Maglia, Energ. Environ. Sci. 11 (2018) 850−859.

[14] Y. Noda, K. Nakano, H. Takeda, M. Kotobuki, L. Lu, M. Nakayama, Tuning mobility and stability of lithium ion conductors based on lattice dynamics, Chem. Mater. 29 (2017) 8983−8991.

[15] H. Wang, R. DeWees, Synthesis and properties of NASICON- type LATP and LAGP solid electrolytes, ChemSusChem 12 (2019) 3713−3725.

[16] L. Buannic, B. Orayech, J.-M. López Del Amo, J. Carrasco, N. A. Katcho, F. d. r. Aguesse, W. Manalastas, W. Zhang, J. Kilner, A. Llordés, Dual substitution strategy to enhance Li^+ ionic conductivity in $Li_7La_3Zr_2O_{12}$ solid electrolyte, Chem. Mater. 29 (2017) 1769−1778.

[17] Y. Kato, S. Hori, T. Saito, K. Suzuki, M. Hirayama, A. Mitsui, M. Yonemura, H. Iba, R. Kanno, High-power all-solid-state batteries using sulfide superionic conductors, Nat. Energy 1 (2016) 16030.

[18] M. Tatsumisago, M. Nagao, A. Hayashi, Recent development of sulfide solid electrolytes and interfacial modification for all-solid-state rechargeable lithium batteries, J. Asian Ceram. Soc. 1 (2013) 17−25.

[19] N. Kamaya, K. Homma, Y. Yamakawa, M. Hirayama, R. Kanno, M. Yonemura, T. Kamiyama, Y. Kato, S. Hama, K. Kawamoto, A lithium superionic conductor, Nat. Mater. 10 (2011) 682.

[20] R. Garcia-Mendez, F. Mizuno, R. Zhang, T. S. Arthur, J. Sakamoto, Effect of Processing Conditions of $75Li_2S$-$25P_2S_5$ Solid electrolyte on its DC electrochemical behavior, Electrochim. Acta 237 (2017) 144−151.

[21] M. Nagao, A. Hayashi, M. Tatsumisago, T. Kanetsuku, T. Tsuda, S. Kuwabata, In Situ SEM study of a lithium deposition and dissolution mechanism in a bulk-type solid-state cell with a Li_2S-P_2S_5 solid electrolyte, Phys. Chem. Chem. Phys. 15 (2013) 18600−18606.

[22] F. Han, J. Yue, X. Zhu, C. Wang, Suppressing Li dendrite formation in Li_2S- P_2S_5 solid electrolyte by LiI incorporation, Adv. Energy Mater. 8 (2018)

1703644.

[23] L. Porz, T. Swamy, B. W. Sheldon, D. Rettenwander, T. Frömling, H. L. Thaman, S. Berendts, R. Uecker, W. C. Carter, Y. M. Chiang, Mechanism of lithium metal penetration through inorganic solid electrolytes, Adv. Energy Mater. 7 (2017) 1701003.

[24] E. J. Cheng, A. Sharafi, J. Sakamoto, Intergranular Li metal propagation through polycrystalline $Li_{6.25}Al_{0.25}La_3Zr_2O_{12}$ ceramic electrolyte, Electrochim. Acta 223 (2017) 85−91.

[25] C.-L. Tsai, V. Roddatis, C. V. Chandran, Q. Ma, S. Uhlenbruck, M. Bram, P. Heitjans, O. Guillon, $Li_7La_3Zr_2O_{12}$ interface modification for Li dendrite prevention, ACS Appl. Mater. Interfaces 8 (2016) 10617−10626.

[26] F. Yonemoto, A. Nishimura, M. Motoyama, N. Tsuchimine, S. Kobayashi, Y. Iriyama, Temperature effects on cycling stability of Li plating/stripping on Ta-doped $Li_7La_3Zr_2O_{12}$, J. Power Sources 343 (2017) 207−215.

[27] K. N. Wood, E. Kazyak, A. F. Chadwick, K. H. Chen, J. G. Zhang, K. Thornton, N. P. Dasgupta, Dendrites and pits: untangling the complex behavior of lithium metal anodes through operando video microscopy, ACS Cent. Sci. 2 (2016) 790−801.

[28] K. N. Wood, M. Noked, N. P. Dasgupta, Lithium metal anodes: toward an improved understanding of coupled morphological, electrochemical, and mechanical behavior, ACS Energy Lett. 2 (2017) 664−672.

[29] K. Ishiguro, H. Nemori, S. Sunahiro, Y. Nakata, R. Sudo, M. Matsui, Y. Takeda, O. Yamamoto, N. Imanishi, Ta-doped $Li_7La_3Zr_2O_{12}$ for water-stable lithium electrode

of lithium-air batteries, J. Electrochem. Soc. 161 (2014) A668−A674.

[30] R. Sudo, Y. Nakata, K. Ishiguro, M. Matsui, A. Hirano, Y. Takeda, O. Yamamoto, N. Imanishi, Interface behavior between garnet-type lithium-conducting solid electrolyte and lithium metal, Solid State Ion. 262 (2014) 151−154.

[31] Y. Lu, Z. Tu, L. A. Archer, Stable lithium electrodeposition in liquid and nanoporous solid electrolytes, Nat. Mater. 13 (2014) 961.

[32] W. Li, H. Yao, K. Yan, G. Zheng, Z. Liang, Y.-M. Chiang, Y. Cui, The synergetic effect of lithium polysulfide and lithium nitrate to prevent lithium dendrite growth, Nat. Commun. 6 (2015) 7436.

[33] L. Grande, J. von Zamory, S. L. Koch, J. Kalhoff, E. Paillard, S. Passerini, Homogeneous lithium electrodeposition with pyrrolidinium-based ionic liquid electrolytes, ACS Appl. Mater. Interfaces 7 (2015) 5950−5958.

[34] Q. Lu, Y. B. He, Q. Yu, B. Li, Y. V. Kaneti, Y. Yao, F. Kang, Q. H. Yang, Dendrite- free, high- rate, long- life lithium metal batteries with a 3D cross- linked network polymer electrolyte, Adv. Mater. 29 (2017) 1604460.

[35] X. Fan, X. Ji, F. Han, J. Yue, J. Chen, L. Chen, T. Deng, J. Jiang, C. Wang, Fluorinated solid electrolyte interphase enables highly reversible solid-state Li metal battery, Sci. Adv. 4 (2018) 9245.

[36] C. Wang, K. R. Adair, J. Liang, X. Li, Y. Sun, X. Li, J. Wang, Q. Sun, F. Zhao, X. Lin, Solid- state plastic crystal electrolytes: effective protection interlayers for sulfide- based all- solid- state lithium metal batteries, Adv. Funct. Mater. 29 (2019) 1900392.

[37] X. Han, Y. Gong, K. K. Fu, X. He, G. T. Hitz, J. Dai, A. Pearse, B. Liu, H. Wang, G. Rubloff, Negating interfacial impedance in garnet-based solid-state Li metal batteries, Nat. Mater. 16 (2017) 572.

[38] A. Sharafi, H. M. Meyer, J. Nanda, J. Wolfenstine, J. Sakamoto, Characterizing the Li-$Li_7La_3Zr_2O_{12}$ interface stability and kinetics as a function of temperature and current density, J. Power Sources 302 (2016) 135−139.

[39] A. Sharafi, E. Kazyak, A. L. Davis, S. Yu, T. Thompson, D. J. Siegel, N. P. Dasgupta, J. Sakamoto, Surface chemistry mechanism of ultra-low interfacial resistance in the solid-state electrolyte $Li_7La_3Zr_2O_{12}$, Chem. Mater. 29 (2017) 7961−7968.

[40] X.-B. Cheng, R. Zhang, C.-Z. Zhao, Q. Zhang, Toward safe lithium metal anode in rechargeable batteries: a review, Chem. Rev. 117 (2017) 10403−10473.

[41] Y. Zhang, W. Luo, C. Wang, Y. Li, C. Chen, J. Song, J. Dai, E. M. Hitz, S. Xu, C. Yang, High-capacity, low-tortuosity, and channel-guided lithium metal anode, Proc. Natl. Acad. Sci. 114 (2017) 3584−3589.

[42] M. H. Ryou, D. J. Lee, J. N. Lee, Y. M. Lee, J. K. Park, J. W. Choi, Excellent cycle life of lithium- metal anodes in lithium- ion batteries with mussel- inspired polydopamine- coated separators, Adv. Energy Mater. 2 (2012) 645−650.

[43] S. H. Wang, Y. X. Yin, T. T. Zuo, W. Dong, J. Y. Li, J. L. Shi, C. H. Zhang, N. W. Li, C. J. Li, Y. G. Guo, Stable Li metal anodes via regulating lithium plating/stripping in vertically aligned microchannels, Adv. Mater. 29 (2017) 1703729.

[44] H. Zhu, W. Luo, P. N. Ciesielski, Z. Fang, J. Zhu, G. Henriksson, M. E. Himmel,

L. Hu, Wood-derived materials for green electronics, biological devices, and energy applications, Chem. Rev. 116 (2016) 9305−9374.

[45] H. Song, S. Xu, Y. Li, J. Dai, A. Gong, M. Zhu, C. Zhu, C. Chen, Y. Chen, Y. Yao, B. Liu, J. Song, G. Pastel, L. Hu, Hierarchically porous, ultrathick, "breathable" wood- derived cathode for lithium- oxygen batteries, Adv. Energy Mater. 8 (2018) 1701203.

[46] Y. Li, K. K. Fu, C. Chen, W. Luo, T. Gao, S. Xu, J. Dai, G. Pastel, Y. Wang, B. Liu, J. Song, Y. Chen, C. Yang, L. Hu, Enabling high-areal-capacity lithium-sulfur batteries: designing anisotropic and low-tortuosity porous architectures, ACS Nano 11 (2017) 4801−4807.

[47] J. Dai, K. Fu, Y. Gong, J. Song, C. Chen, Y. Yao, G. Pastel, L. Zhang, E. Wachsman, L. Hu, Flexible solid-state electrolyte with aligned nanostructures derived from wood, ACS Mater. Lett. 1 (2019) 354−361.

[48] L. L. Lu, Y. Y. Lu, Z. J. Xiao, T. W. Zhang, F. Zhou, T. Ma, Y. Ni, H. B. Yao, S. H. Yu, Y. Cui, Wood- inspired high- performance ultrathick bulk battery electrodes, Adv. Mater. 30 (2018) 1706745.

[49] W. Liu, S. W. Lee, D. Lin, F. Shi, S. Wang, A. D. Sendek, Y. Cui, Enhancing ionic conductivity in composite polymer electrolytes with well-aligned ceramic nanowires, Nat. Energy 2 (2017) 1−7.

[50] X. Wang, H. Zhai, B. Qie, Q. Cheng, A. Li, J. Borovilas, B. Xu, C. Shi, T. Jin, X. Liao, Y. Li, X. He, S. Du, Y. Fu, M. Dontigny, K. Zaghib, Y. Yang, Rechargeable

solid-state lithium metal batteries with vertically aligned ceramic nanoparticle/polymer composite electrolyte, Nano Energy 60 (2019) 205−212.

[51] J. Wan, J. Xie, X. Kong, Z. Liu, K. Liu, F. Shi, A. Pei, H. Chen, W. Chen, J. Chen, X. Zhang, L. Zong, J. Wang, L. Q. Chen, J. Qin, Y. Cui, Ultrathin, flexible, solid polymer composite electrolyte enabled with aligned nanoporous host for lithium batteries, Nat. Nanotechnol. 14 (2019) 705−711.

[52] Z. Jiang, H. Xie, S. Wang, X. Song, X. Yao, H. Wang, Perovskite membranes with vertically aligned microchannels for all- solid- state lithium batteries, Adv. Energy Mater. 8 (2018) 1801433.

[53] C. Yu, S. Ganapathy, N. J. de Klerk, I. Roslon, E. R. van Eck, A. P. Kentgens, M. Wagemaker, Unravelling Li-ion transport from picoseconds to seconds: bulk versus interfaces in an argyrodite Li_6PS_5Cl-Li_2S all-solid-state Li-ion battery, J. Am. Chem. Soc. 138 (2016) 11192−11201.

[54] D. A. Ziolkowska, W. Arnold, T. Druffel, M. Sunkara, H. Wang, Rapid and economic synthesis of a Li_7PS_6 solid electrolyte from a liquid approach, ACS Appl. Mater. Interfaces 11 (2019) 6015−6021.

[55] C. Yu, S. Ganapathy, J. Hageman, L. van Eijck, E. R. van Eck, L. Zhang, T. Schwietert, S. Basak, E. M. Kelder, M. Wagemaker, Facile synthesis toward the optimal structure-conductivity characteristics of the argyrodite Li_6PS_5Cl solid-state electrolyte, ACS Appl. Mater. Interfaces 10 (2018) 33296−33306.

[56] J. Li, Y. Lu, D. Yang, Q. Sun, Y. Liu, H. Zhao, Lignocellulose aerogel from wood-ionic liquid solution (1-allyl-3-methylimidazolium chloride) under freezing and

thawing conditions, Biomacromolecules 12 (2011) 1860−1867.

[57] S. Wenzel, S. J. Sedlmaier, C. Dietrich, W. G. Zeier, J. Janek, Interfacial reactivity and interphase growth of argyrodite solid electrolytes at lithium metal electrodes, Solid State Ion. 318 (2018) 102−112.

[58] J. Zhang, Y. Bai, X.-G. Sun, Y. Li, B. Guo, J. Chen, G. M. Veith, D. K. Hensley, M. P. Paranthaman, J. B. Goodenough, Superior conductive solid-like electrolytes: nanoconfining liquids within the hollow structure, Nano Lett. 15 (2015) 3398−3402.

[59] K. K. Fu, Y. Gong, J. Dai, A. Gong, X. Han, Y. Yao, C. Wang, Y. Wang, Y. Chen, C. Yan, Flexible, solid-state, ion-conducting embrane with 3D garnet nanofiber networks for lithium batteries, Proc. Natl. Acad. Sci. 113 (2016) 7094−7099.

[60] J. Auvergniot, A. Cassel, D. Foix, V. Viallet, V. Seznec, R. Dedryvère, Redox activity of argyrodite Li_6PS_5Cl electrolyte in all-solid-state Li-ion battery: an XPS study, Solid State Ion. 300 (2017) 78−85.

[61] H. Chen, A. Pei, D. Lin, J. Xie, A. Yang, J. Xu, K. Lin, J. Wang, H. Wang, F. Shi, Uniform high ionic conducting lithium sulfide protection layer for stable lithium metal anode, Adv. Energy Mater. 9 (2019) 1900858.

[62] Y. Ren, Y. Zhou, Y. Cao, Inhibit of Lithium Dendrite Growth in Solid Composite Electrolyte by Phase-Field Modeling, J. Phys. Chem. C, 124 (2020) 12195-12204.

[63] Z. Liu, W. Fu, A. Payzamy. X. Yu, Z. Wi, N. Dudney, J. Kiggans, K. Hong, A. Rondinone, C. Liang, Anomalous High Ionic Conductivity of Nanoporous β-Li_3PS_4, J. Am. Chem. Soc., 135 (2013), 975-978.

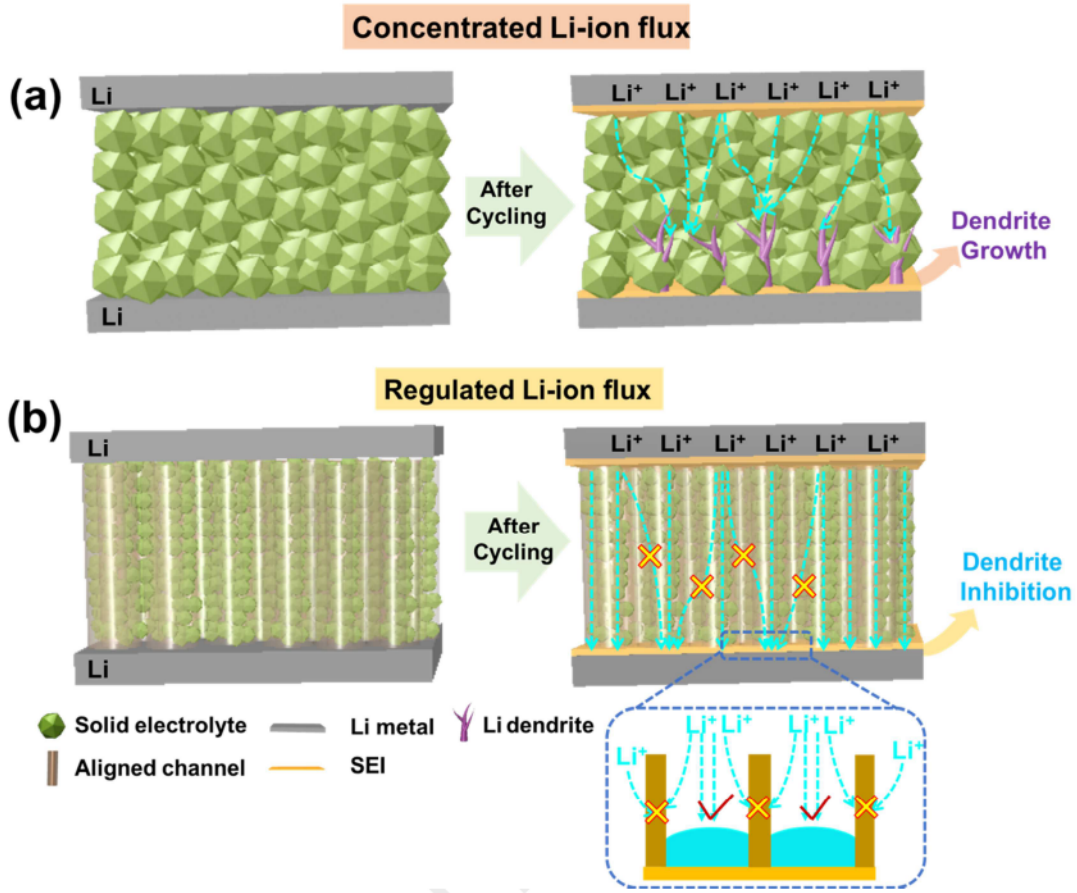

Scheme 1. (a) Li metal anode with bare SE. In bare SE, concentrated Li ionic flux results in inhomogeneous Li stripping/plating. Li deposits further accumulate at the spots where the current density is locally enhanced and finally evolve into Li dendrites. (b) SE structure containing aligned channels. With channels, Li ionic flux in SE could be confined in each channel, leading to a homogeneous Li electrodeposition behavior and thus uniform Li nucleation/growth, which results in Li dendrite inhibition.

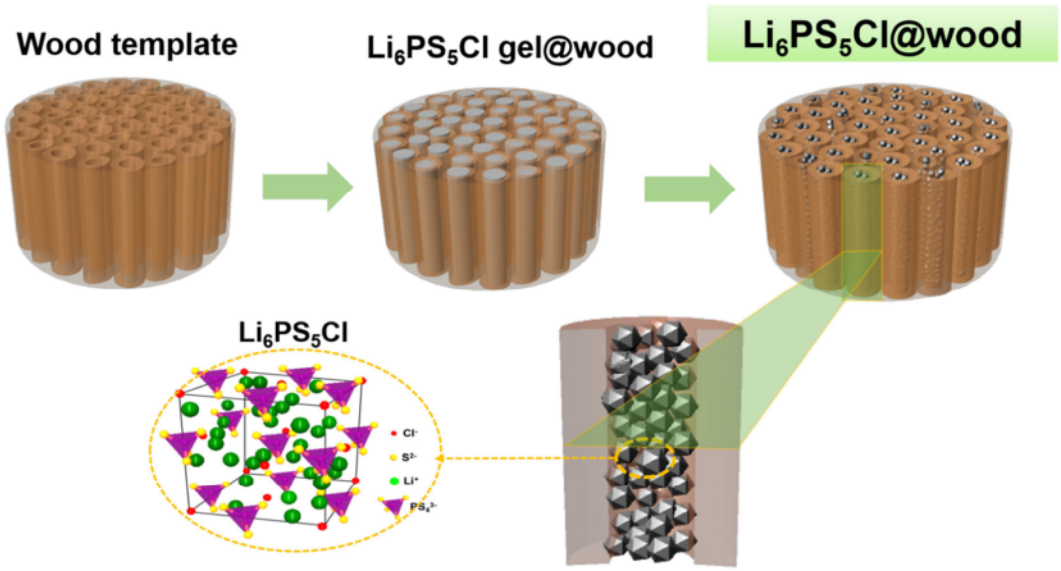

Scheme 2. Graphical diagrams for the fabrication of Li_6PS_5Cl@wood SE from wood template and the crystalline structure of Li_6PS_5Cl.

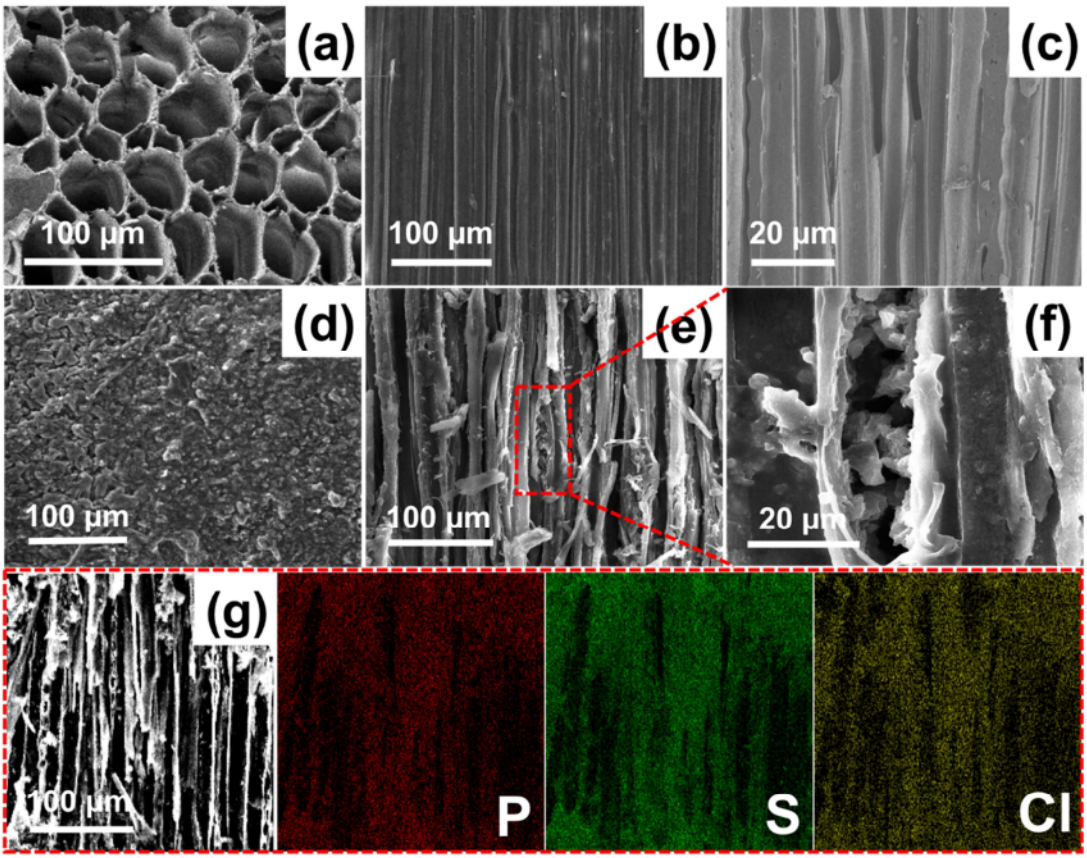

Fig. 1. (a–c) Top-view and cross-sectional SEM images of wood template present typical well-aligned channel structure with average diameters of around 15 μm. (d–f) SEM images of top surface and cross-section of Li_6PS_5Cl@wood SE infused with SE in wood channels. Crystalline Li_6PS_5Cl can be clearly seen in the wood channels. (g) EDS mappings of P, S and Cl distributions in Li_6PS_5Cl@wood SE, which indicates SE uniformly infused in wood template.

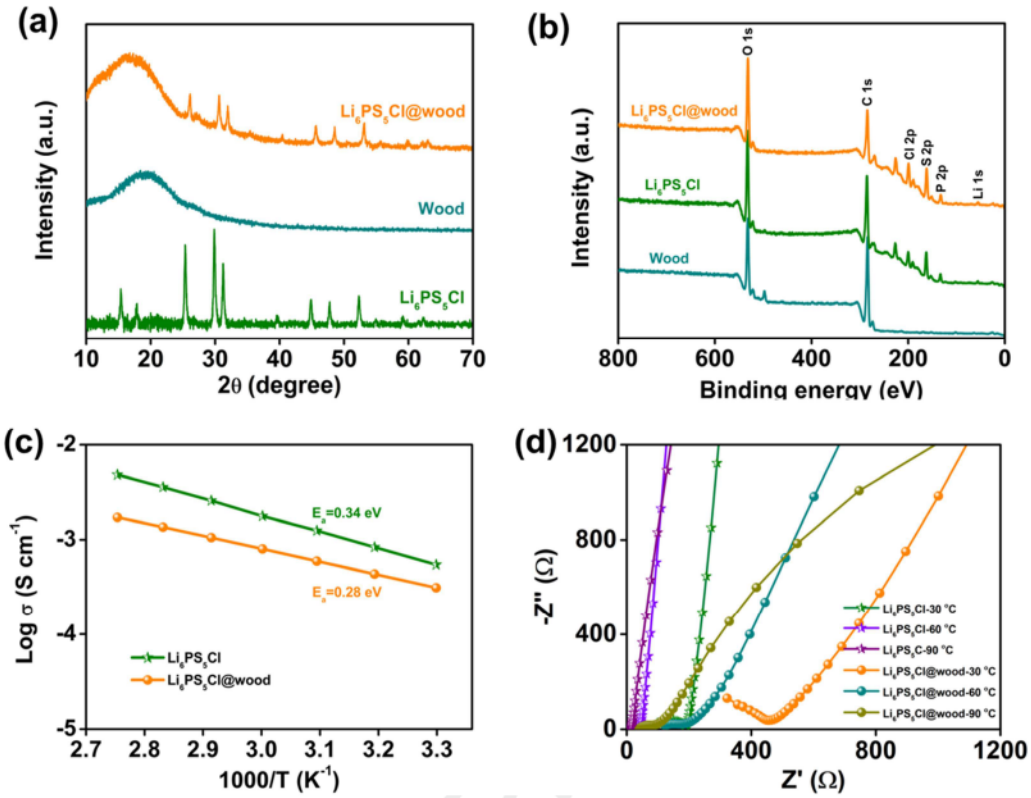

Fig. 2. (a,b) XRD patterns and XPS spectra of pure Li_6PS_5Cl, pristine wood and Li_6PS_5Cl@wood SE. Li_6PS_5Cl exhibits argyrodite cubic structure (space group *F-43m*), which is well defined in Li_6PS_5Cl@wood sample. (c) Arrhenius plots of Li_6PS_5Cl and Li_6PS_5Cl@wood SEs. Activation energy (E_a) is 0.28 eV for Li_6PS_5Cl@wood SE and 0.34 eV for Li_6PS_5Cl SE. (d) EIS spectra of Li_6PS_5Cl and Li_6PS_5Cl@wood SEs at various temperatures of 30, 60 and 90 °C.

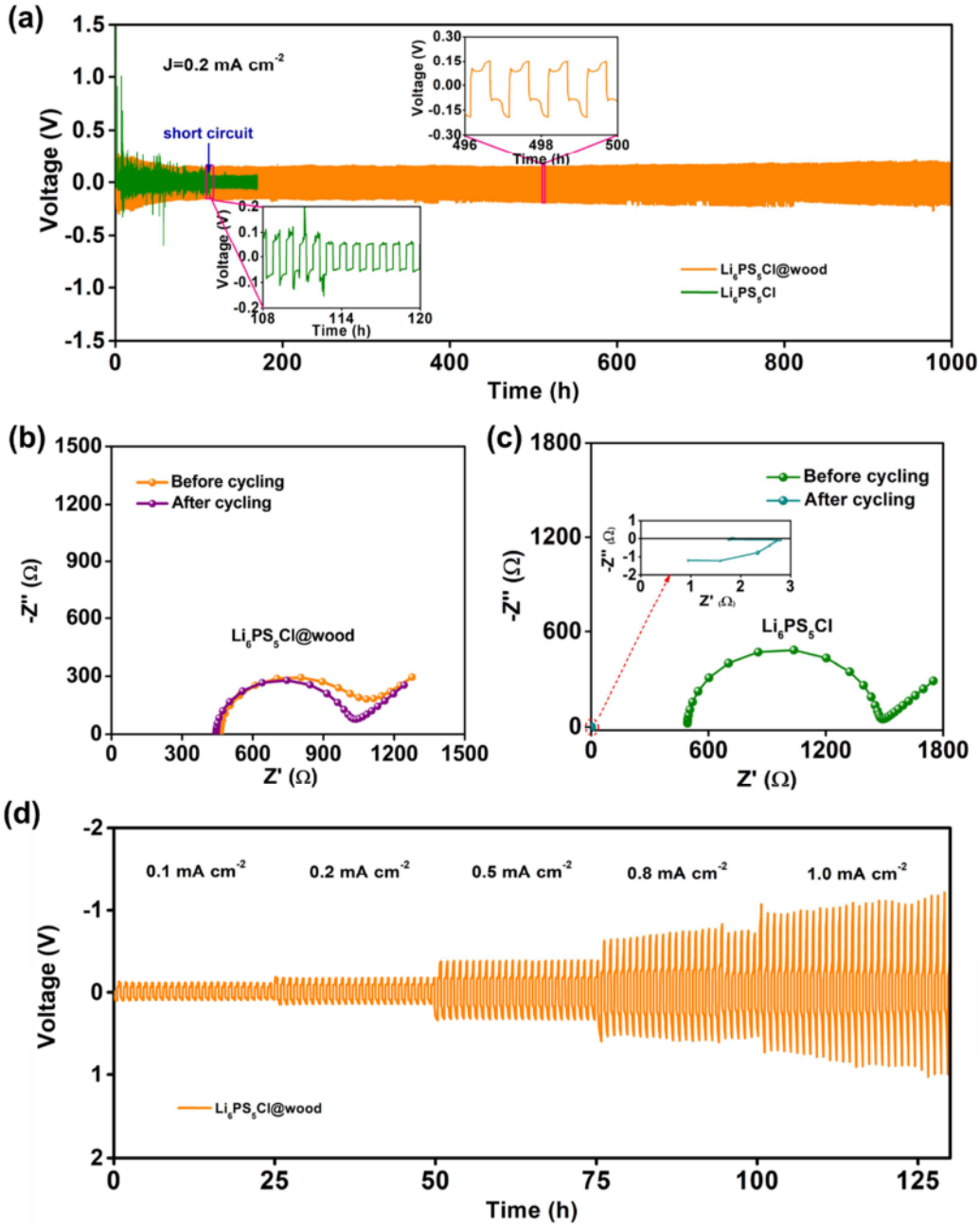

Fig. 3. (a) Voltage profiles of symmetric cells for Li_6PS_5Cl (green) and Li_6PS_5Cl@wood (orange) SEs at current density of 0.2 mA cm^{-2} with a fixed areal capacity of 0.1 mAh cm^{-2}. Insets are zoomed-in profiles of typical cycles. Compared with bare Li_6PS_5Cl, Li_6PS_5Cl@wood SE exhibited long-term cycling stability without short-circuit. EIS spectra of symmetric cells with (b) Li_6PS_5Cl@wood and (c) Li_6PS_5Cl SEs before and after cycling. (d) Voltage profiles of symmetric

Li|Li_6PS_5Cl@wood|Li cell cycled at various current densities of 0.1, 0.2, 0.5, 0.8 and 1.0 mA cm^{-2}, which correspond to the areal capacities of 0.05, 0.1, 0.25, 0.4 and 0.5 mAh cm^{-2}, respectively.

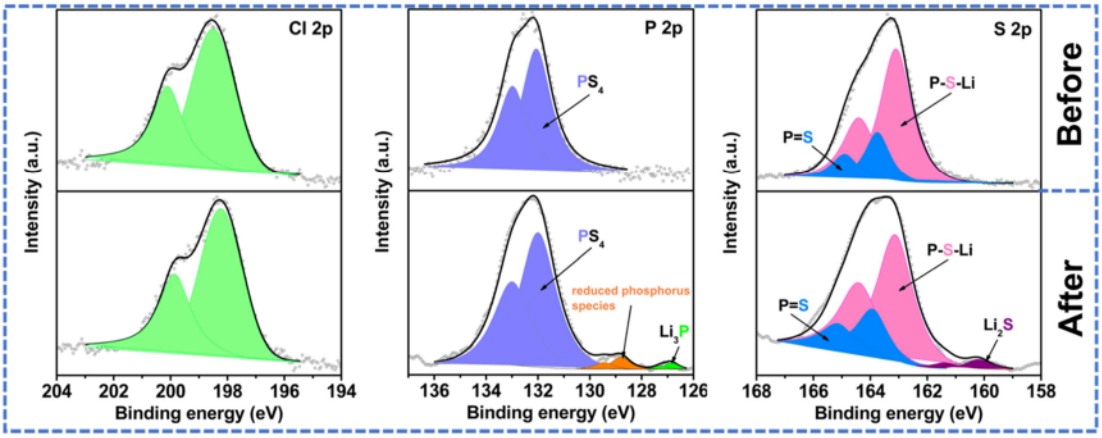

Fig. 4. Detailed XPS spectra and peak fits of Cl 2p, P 2p and S 2p for the Li_6PS_5Cl@wood SE before and after cycling. Interphase containing species of Li_2S and Li_3P formed after cycling.

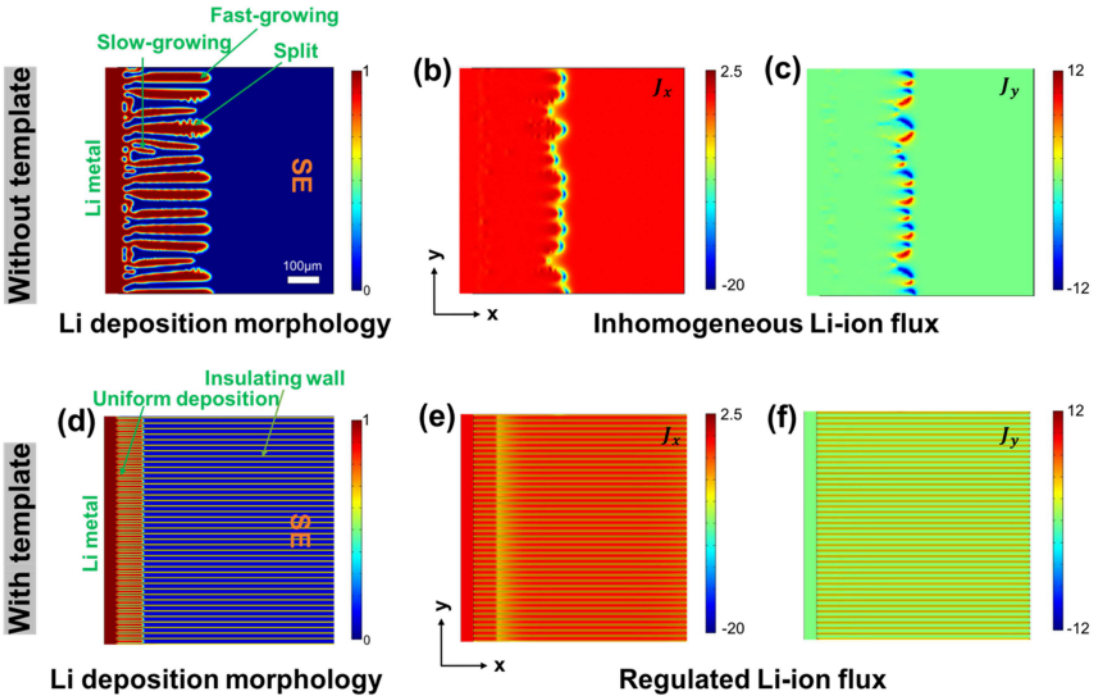

Fig. 5. Phase-field simulation of Li deposition in SE described by a phase-field variable (ξ), where ξ = 1.0 for Li metal and ξ = 0.0 for SE. Phase-field simulation of Li ion flux (J) in SE investigated along vertical (x) direction (J_x) and horizontal (y) direction (J_y). (a–c) Li deposition morphology and Li-ion flux distribution in bare Li_6PS_5Cl SE. Inhomogeneous Li dendrite growth in SE without template. (d–f) Li deposition morphology and Li-ion flux distribution in Li_6PS_5Cl@wood SE. Homogeneous Li deposits in the aligned channels. The scale bar in (a) applies to (b–f).

Declaration of interests

☒ The authors declare that they have no known competing financial interests or personal relationships that could have appeared to influence the work reported in this paper.

☐The authors declare the following financial interests/personal relationships which may be considered as potential competing interests: